



# Space-time simulation of intermittent rainfall with prescribed advection field: Adaptation of the turning band method

E. Leblois, J.D. Creutin

## ► To cite this version:

E. Leblois, J.D. Creutin. Space-time simulation of intermittent rainfall with prescribed advection field: Adaptation of the turning band method. *Water Resources Research*, 2013, 39, p. 3375 - p. 3387. 10.1002/wrcr.20190 . hal-01073172

**HAL Id: hal-01073172**

**<https://hal.science/hal-01073172>**

Submitted on 9 Oct 2014

**HAL** is a multi-disciplinary open access archive for the deposit and dissemination of scientific research documents, whether they are published or not. The documents may come from teaching and research institutions in France or abroad, or from public or private research centers.

L'archive ouverte pluridisciplinaire **HAL**, est destinée au dépôt et à la diffusion de documents scientifiques de niveau recherche, publiés ou non, émanant des établissements d'enseignement et de recherche français ou étrangers, des laboratoires publics ou privés.

## Space-time simulation of intermittent rainfall with prescribed advection field: Adaptation of the turning band method

Etienne Leblois<sup>1</sup> and Jean-Dominique Creutin<sup>2</sup>

Received 6 December 2011; revised 7 March 2013; accepted 8 March 2013; published 14 June 2013.

[1] Space-time rainfall simulation is useful to study questions like, for instance, the propagation of rainfall-measurement uncertainty in hydrological modeling. This study adapts a classical Gaussian field simulation technique, the turning-band method, in order to produce sequences of rainfall fields satisfying three key features of actual precipitation systems: (i) the skewed point distribution and the space-time structure of nonzero rainfall (NZR); (ii) the average probability and the space-time structure of intermittency; and (iii) a prescribed advection field. The acronym of our simulator is SAMPO, for simulation of advected mesoscale precipitations and their occurrence. SAMPO assembles various theoretical developments available from the literature. The concept of backtrajectories introduces a priori any type of advection field in the heart of the turning band method (TBM). TBM outputs transformation into rainfall fields with a desired structure is controlled using Chebyshev-Hermite polynomial expansion. The intermittency taken as a binary process statistically independent of the NZR process allows the use of a common algorithm for both processes. The 3-D simulation with a space-time anisotropy captures important details of the precipitation kinematics summarized by the Taylor velocity of both NZR and intermittency. A case study based on high-resolution weather radar data serves as an example of model inference. Illustrative simulations revisit some classical questions about rainfall variability like the influence of advection or intermittency. They also show the combined role of Taylor's and advection velocities.

**Citation:** Leblois, E., and J.-D. Creutin (2013), Space-time simulation of intermittent rainfall with prescribed advection field: Adaptation of the turning band method, *Water Resour. Res.*, 49, 3375–3387, doi:10.1002/wrcr.20190.

### 1. Introduction

[2] In hydrology, the very fact motivating the simulation of rainfall fields is to understand how the hierarchy of river basins collects rainfall at ground and transforms rainfall variability into runoff variability. For instance, recent works studied the influence of rainfall variability on the hydrologic response in general [Vischel *et al.*, 2009] and on more specific features like the scaling structure of peak flows [Mandapaka *et al.*, 2009]. In this perspective, hydrologic regimes are seen as the transformation of climate through rainfall-runoff conversion processes (see for instance, Gupta *et al.* [1996] for the basis of a physical-statistical theory of regional floods or Menabde and Sivapalan [2001]). The finality of these studies covers both water resource management and water-related hazards.

[3] A variety of numerical models generate rainfall fields. The outputs of global climate models allowed hydrological studies at continental scale [Arnell, 1999]. To use these outputs at finer regional scales, statistical and dynamical downscaling methodologies have been used to refine the space-time description of rainfall variability [Boé *et al.*, 2009; Mezghani and Hingray, 2009]. A distinct body of works promoted ad hoc stochastic simulators replicating the statistical properties of historical rainfall data sets. For instance, Amorcho and Wu [1977] proposed the initial concept of rain cell clusters organized in storm bands used by the family of so-called space-time models. Mejia and Rodriguez-Iturbe [1974] and Bell [1987] developed two-dimensional isotropic models generating correlated random fields using spectral analysis, initiating the so-called meta-Gaussian model family.

[4] The simulator proposed in this study contributes to the stochastic approach with the particularity of adapting a classical Gaussian random field generator, the turning band method (TBM), to simulate advected intermittent rainfall fields. The assumptions made are intimately related to the time and space resolution of the simulated fields. Our ambition is to simulate rainfall fields at a resolution of typically 10 min and 1 km<sup>2</sup> over domains of several thousands of square kilometers, where intermittency and advection are relevant features.

[5] Compared to the use of historical data sets, a stochastic simulator better fits various hydrological needs. Through a set of theoretical assumptions, it reproduces statistical properties that are consistent with observed data (mean,

Additional supporting information may be found in the online version of this article.

<sup>1</sup>Irstea Lyon, HHLY Research Unit, Villeurbanne, France.

<sup>2</sup>CNRS/UJF-Grenoble 1/G-INP/IRD, Laboratoire d'étude des Transferts en Hydrologie et Environnement, LTHE, UMR 5564, Grenoble, France.

Corresponding author: E. Leblois, Irstea Lyon, 5 Rue de la Doua, CS 70077, F-69626 Villeurbanne Cedex, France. (etienne.leblois@irstea.fr)

©2013. American Geophysical Union. All Rights Reserved.  
0043-1397/13/10.1002/wrcr.20190

variance, correlation length in time and space, etc.). It offers data better resolved in space and time. It covers the long run and allows the generation of multiple sets of fields. It thus helps to step back from the peculiarities of a reduced number of events or, worse, of a single “project event.” This gives better account of natural rainfall variability. In conditional simulation mode, it offers ways to represent uncertainties linked to measurement or sampling and to study their propagation through hydrological modeling. The control of the simulation assumptions allows investigating individual effects of such or such observed rainfield property, in particular, when they are expected to change in intensity or frequency.

[6] Our software is available under the name SAMPO, an acronym for simulation of advected mesoscale precipitations and their occurrence. It is more specific to rainfall than existing TBM simulators like HYDRO-GEN [Bellin and Rubin, 1996] or the TBSim suite [Emery and Lantuéjoul, 2006]. This article concentrates on the generation of rainfall sequences of homogenous type, i.e., with constant statistical properties. The part of SAMPO creating the climatological succession of rainfall types through a hidden Markov model is not presented here.

[7] The TBM has been introduced in its general form by Matheron [1973] and popularized for 2-D applications in hydrology by Mantoglou and Wilson [1982]. The simulation performs orthogonal backprojections in a multidimensional space of a number of 1-D autocorrelated processes generated along randomly oriented lines. Each individual line process yields by backprojection perpendicular stripes of equal values—the turning bands that gave its name to the method. The accumulation of these bands generates a multidimensional Gaussian random field that is statistically homogeneous. The choice of the covariance function of the line process controls the final structure of the multidimensional field.

[8] To simulate advected intermittent rainfall fields, the TBM needs to be adapted regarding the following issues. First, rainfall distribution is skewed toward high values almost at all time scales, and thus non-Gaussian. In this study, we use the inverse Gaussian distribution [Chhikara and Folks, 1974; Folks and Chhikara, 1978]. Its main advantages are to deal with positive values, to have a reduced number of parameters (two), and to fairly behave for extremes (asymptotic exponential behavior of block-maximum values close to Gumbel). Journel and Huijbregts [1978] proposed to simulate non-Gaussian fields applying an anamorphosis transformation to Gaussian fields. The anamorphosis is known to modify the structure of the field. The underlying Gaussian structure has to be consistent with the targeted structure of the transformed field.

[9] Second, rainfall fields are advected by the atmospheric dynamics in a deterministic way that should also be introduced in a simulator. Advection is a simplified view that holds when the horizontal atmospheric organization (saturated layers, condensation level, pressure gradient) controls convective activity. The space and time resolution of weather radar images evidenced this horizontal movement of rainfall patterns better than rain gauge networks. Zawadzki [1973] studied the space-time correlation of precipitation patterns using this concept, which has been also used to produce short-term forecasting [Austin and Bellon,

1974] and to improve conventional rainfall observation at fixed points [Niemczynowicz, 1988]. In fluid mechanics, the notions of stream function and particle trajectory in stationary or incompressible fields can help to define advection fields that are physically consistent.

[10] Third, rainy areas do not fill the entire space in most cases and intermittency must also be simulated. A possible choice is to use a truncated distribution with a finite probability allocated to zero rainfall in the anamorphosis transformation [Bardossy, 2011]. We made an alternate choice considering that intermittency and inner rainfall variability are independent random fields [Barancourt et al., 1992]. The intermittent rainfall field is obtained by multiplying a nonzero rainfall (NZR) field covering the entire space by a binary mask (a thresholded Gaussian field following Galli et al. [1994]).

[11] The general formulation of the intermittent rainfall fields  $R_I$  proposed in this paper will take the following form (see section 6):

$$R_I(\mathbf{x}_E, t) = \varphi(Y_R(\mathbf{x}_L, t, U_R)) \mathbf{1}_{Y_I(\mathbf{x}_L, t, U_I) \geq \lambda}, \quad (1)$$

where  $Y_R$  and  $Y_I$  are the two independent Gaussian functions used to represent NZR and intermittency with  $U_R$  and  $U_I$  featuring their respective dynamics;  $\varphi$  stands for the anamorphosis used to care about the skewed distribution;  $\lambda$  characterizes the fraction of intermittency; the combined use of Lagrangian  $\mathbf{x}_L$  and Eulerian  $\mathbf{x}_E$  coordinates takes care about advection. The separate specification of NZR, intermittency and advection is easy to carry on and gives flexibility to control the properties of the resulting compound field.

[12] Our paper is organized as follows. Section 2 describes the kinematics of atmospheric flow implemented in SAMPO. Sections 3 and 4 give a short description of the TBM and detail how the simulator preserves the correct structure when simulating non-Gaussian distributions. Using Eulerian and Lagrangian perspectives Section 5 shows how Taylor velocity combines to advection to generate rainfall kinematics. Section 6 extends the simulation to intermittency fields. Section 7 describes the practical details of the simulator implementation for advected non-Gaussian rainfall fields using a high-resolution radar data set. Section 8 uses the simulator to revisit some classical questions about rainfall variography, such as how rainfall accumulation over time and advection influence experimental variograms. It also illustrates the kinematic effect obtained merging advection and Taylor velocity. Section 9 is the conclusion.

## 2. Kinematic Description of the Advection Field

[13] Our simulator considers that rainfield kinematics results from the advection of a stochastic process producing rain in a Lagrangian space. From a meteorological standpoint it assumes that the convective activity producing rain is independent of the horizontal wind field advecting the rain patterns. In practice, the Lagrangian rain production is simulated with a 3-D TBM in which the correlation structure in time is scaled in relation to space following the Taylor approach (see section 5). The horizontal wind field controlling advection is prescribed either from observed or simulated data. In order to have a self-consistent basic tool

to reproduce the kinematics of advection in the absence of data, we propose below a simplified parametric description.

[14] The advection  $\mathbf{U}(\mathbf{x}, t)$  depends on the location  $\mathbf{x}$  with  $\mathbf{x}=(x, y)$  and the time  $t$  and has components  $u(\mathbf{x}, t)$  and  $v(\mathbf{x}, t)$  along the axes  $Ox$  and  $Oy$ , respectively. The Eulerian observer can describe at any time the current lines (lines not crossed by the flux) integrating the differential equation  $dx/u=dy/v$ . The Lagrangian observer follows a noninertial particle  $(\mathbf{x}_0, t_0)$ , passing at location  $\mathbf{x}_0$  at time  $t_0$ . At time  $t_1$  it will reach the location  $\mathbf{x}_1$  with

$$\mathbf{x}_1 = \mathbf{x}_0 + \int_{t_0}^{t_1} \mathbf{U}(\mathbf{x}_t, t) dt, \quad (2)$$

where the union of locations  $(\mathbf{x}_t)$  followed by the integral is the trajectory of the particle, which is confounded with the current line in steady flow only.

[15] A convenient way to specify an incompressible advection field is to equal its divergence to zero:

$$\text{div } \mathbf{U} = \frac{\partial u}{\partial x} + \frac{\partial v}{\partial y} = 0. \quad (3)$$

[16] Let us define  $\mathbf{U}$  as curl  $(\psi)$  with any scalar twice-differentiable function of location and time. The vector  $\mathbf{U}(\mathbf{x}, t)$  will have the following components:

$$u = \frac{\partial \psi}{\partial y} \text{ and } v = -\frac{\partial \psi}{\partial x}. \quad (4)$$

[17] As  $\text{div } (\mathbf{U}) = \text{div } (\text{curl } (\psi)) = 0$ , we verify that any scalar function  $\psi$  of class  $\mathbf{C}^2$  determines an incompressible advection vector  $\mathbf{U}$  as defined in (3).  $\psi$  is the stream function of the 2-D advection field. Taking  $\psi$  as a polynomial function of order zero (no advection), one (uniform advection) or two (circular and other conic-like fields—ellipses, parabolas, hyperbolas) provides a variety of possible wind fields. Considering that any function  $\psi$  can be locally approximated by a polynomial function, we understand that these basic functions already cover many possible situations, at least at local scale. More sophisticated circulations can be defined using stream functions like, for example,  $\psi = a.e^{-r^2/b^2}$ , where  $a$  and  $b$  are constants and  $r$  is the distance to the vortex center. The sum of two scalar fields  $\psi_1$  and  $\psi_2$  yields a combination of two advection fields (from the linearity of partial derivatives). This is a way to simulate more complex fields with, in particular, the possibility to add local-scale random fluctuations on the top of a synoptic scale advection field coming from either observations or numerical models. These components of the advection field can be time dependent.

### 3. TBM Simulation of Gaussian 3-D Random Fields

[18] The TBM relies on the existence of a univocal relationship between the covariance  $C_l(r)$  of a 1-D random process  $T(s)$  along an arbitrary oriented line of coordinate  $s$  and the covariance  $C_n(r)$  of the  $n$ -D isotropic Gaussian random process  $Y(\mathbf{x})$  resulting from the orthogonal backprojection

of  $T(s)$  in  $\mathbf{R}^n$  (Matheron [1973, p. 462], cited by Emery and Lantuéjoul [2006]). In 3-D, it reads

$$C_1(r) = \frac{d}{dr} [r C_3(r)] \quad (5)$$

where  $r$  is the Euclidian distance separating two points.

[19] The TBM principle thus consists in (i) generating line processes  $T_i$  of chosen covariance in  $N$  directions with  $i=1, N$ , (ii) summing at each point  $(x, y, z)$ , the values back-projected from the  $N$  line processes, and (iii) normalizing by a factor  $1/\sqrt{N}$ .

[20] Our simulator chooses the line directions over the unit sphere of  $\mathbf{R}^3$  either according to random longitudes versus random sinus of the latitude or following a low-discrepancy sequence [Halton, 1964]. It generates the line process from a white noise made of independent and identically distributed (IDD) Gaussian deviates with zero mean and unit variance, separated by a chosen step  $\Delta s$ . The desired covariance  $C_l$  is introduced through a weighted moving average or an autoregressive transformation. In both cases, a set of weights is determined in relation with this covariance. The set of  $K+1$  moving average weights  $w_{\text{MA}}(k)$  is such that

$$C_1(\delta \Delta s) = \sum_{k=0}^{+K} w_{\text{MA}}(k) w_{\text{MA}}(k + \delta), \quad (6)$$

where  $K$  is large enough to reach the correlation extinction. The sum of the weight squares is taken equal to the variance. The set of  $K+1$  autoregression coefficients  $w_{\text{AR}}(k)$  applied to the  $K$  previous points and to the local noise value are given by the Yule-Walker system:

$$\begin{cases} \sum_{k'=1}^K C_1(|k' - k| \Delta s) w_{\text{AR}}(k) = C_1(k \Delta s) & \text{for } k = 1, K, \\ w_{\text{AR}}(0) = \sqrt{C_1(0) - \sum_{k=1}^K w_{\text{AR}}(k) C_1(k \Delta s)}. \end{cases} \quad (7)$$

[21] Equations (5)–(7) are the basis of the weighting schemes found in the literature to generate standard covariance models like exponential or spherical [Journel and Huijbregts, 1978]. More advanced approaches exist [Lantuéjoul, 2002, p. 196; Emery and Lantuéjoul, 2006].

[22] The generated 3-D process  $Y(x, y, z)$  is the following normalized sum:

$$Y(x, y, z) = \frac{1}{\sqrt{N}} \sum_i T_i(s_{x,y,z}^i), \quad (8)$$

where  $s_{x,y,z}^i$  is the orthogonal projection of  $(x, y, z)$  on the  $i$ th line. Coming from  $N$  independent processes, the cumulated values  $Y(x, y, z)$  are IDD and Gaussian. They have a null expected value and a variance  $C_3(0)$ .

### 4. Asymmetric Distribution of NZR

[23] As stated in section 1, for rainfall studies we need an anamorphosis function  $\phi$  transforming a simulated Gaussian



field  $Y_R$  into a field  $R = \phi(Y_R)$  representing the NZR intensity with a non-Gaussian marginal distribution  $F$ . We detail below how to specify the Gaussian field covariance  $C_{Y_R}$  in order to get the desired covariance  $C_{\phi(Y_R)}$  for the non-Gaussian field  $R$ .

[24] To simplify notations in what follows, we leave the coordinates  $(x, y, z)$  or  $(\mathbf{x}, t)$  when they are not needed. Let  $F(r)$  be the cumulative distribution function of the non-Gaussian random variable  $R$ . The reciprocal function, or quantile function,  $F^{-1}(p)$  can be expressed as

$$r = F^{-1}(p) = \varphi(G^{-1}(p)), \quad (9)$$

where  $\phi$  is the anamorphosis function,  $G^{-1}$  is the reciprocal of the Normal distribution function, and  $0 < p < 1$ .

[25] The proposed simulator uses the Chebyshev-Hermite polynomial expansion to approximate the anamorphosis function. The development used is directly inspired from an algorithm dealing with multivariate distributions with correlated marginals [Van der Geest, 1998]. Other derivations do exist (see for instance, Vio et al. [2001, 2002], Guillot [1999], and referenced articles and books). Referring to the theorem of Lancaster, Van der Geest [1998] recalls that the correlation coefficient  $\rho_G$  between a pair of variables  $(G_1, G_2)$  following a bivariate Gaussian distribution and the correlation coefficient  $\rho_F$  between transformed non-Gaussian variables  $F_1$  and  $F_2$ , relate as follows:

$$\rho_F = \sum_{i=1}^{\infty} a_i b_i \rho_G^i, \quad (10)$$

where  $a_i$  and  $b_i$  are the coefficients of the Chebyshev-Hermite expansions of  $F_1$  and  $F_2$ , respectively, starting with  $i = 1$ . In this work, we use standardized Chebyshev-Hermite polynomials with positive leading coefficient defined in relation to successive derivatives of the Gaussian probability density function  $g(x)$  by

$$H_n(x) = \frac{(-1)^n}{\sqrt{n!}} \frac{1}{g(x)} \frac{d^n}{dx^n} g(x). \quad (11)$$

[26] These polynomial coefficients satisfy the following recursion:

$$\begin{aligned} H_0 &= 1; H_1 = X; \text{ for } n \geq 2 : \\ H_n &= \frac{1}{\sqrt{n}} (X \cdot H_{n-1} - (n-1) H'_{n-2}). \end{aligned} \quad (12)$$

[27] This family of polynomials is orthonormal with respect to the Gaussian distribution, which can be written as follows:

$$\int_{-\infty}^{+\infty} H_i(x) H_j(x) g(x) dx = \delta_{ij}, \quad (13)$$

where  $\delta_{i=j} = 1$  and  $\delta_{i \neq j} = 0$ . The expansion of  $R$  takes the form

$$R = \varphi(Y_R) \approx \sum_{i=0}^{\infty} a_i H_i(Y_R), \quad (14)$$

where  $a_0$  is the expected value  $E(R)$ , and the other coefficients  $a_i$  are computed using the following equation:

$$a_i = \int_{x=-\infty}^{+\infty} \varphi(x) H_i(x) g(x) dx \quad \text{for } i > 0, \quad (15)$$

with  $\sum_{i \geq 1} a_i^2 = \text{Var}(R)$ , the variance of  $R$ , a point to check when the weights are numerically evaluated or when the expansion is truncated. In addition, we can notice that  $R_1$  and  $R_2$  having the same expansion, equation (10) now reads:

$$\rho_R = \sum_{i=1}^{\infty} a_i^2 \rho_{Y_R}^i. \quad (16)$$

[28] An appropriate polynomial approximation of the anamorphosis function thus leads to a relationship between the correlation coefficients of, respectively, the bivariate Gaussian and the transformed values.

[29] In practice, the coefficients of the Chebyshev-Hermite polynomial expansion are derived from equation (15). Afterward, they are used to compute the covariance function  $C_{Y_R}$  needed for the Gaussian field  $Y_R$  from the desired covariance  $C_R$ , inverting equation (16) for a discrete series of distances  $r$ . Then, the 1-D covariance function  $C_1$  and the corresponding weights  $w(k)$  are either optimized via the simplex method according to equation (6) for the moving average or directly computed from equation (7) for the autoregression. SAMPO offers the two options, the moving average being preferred in the case of strictly finite covariance range (spherical model). A checking plot is proposed to SAMPO users displaying the tuned weighting system  $w(k)$  together with the prescribed and fitted covariance functions (see Figure 1). One can notice the significant difference due to the anamorphosis between the desired non-Gaussian covariance and the Gaussian covariance used in the TBM. Optimization difficulties can occur from the incompatibility between the models of point rainfall distribution and the covariance function. For instance, according to Matheron [1989], Armstrong [1992], and Lantuéjoul (personal communication), exponential variograms are compatible with almost all distribution models when spherical variograms are less tolerant.

[30] The quantile function  $F^{-1}$  is also needed to compute rain values. When it has no analytical expression, as it is the case for the inverse Gaussian, SAMPO builds a lookup table. Interpolation in the table proves to be faster than a dichotomic search on the cumulative distribution function and more precise than the polynomial approximation of the anamorphosis function  $\phi$  based on its Chebyshev-Hermite expansion.

## 5. Time Anisotropy and Advection of Rainfall Fields

[31] The adaptation to rainfall of the simulation technique described in sections 3 and 4 calls for the following three complementary issues: (i) to introduce an appropriate anisotropy to define time along the third axis, (ii) to describe the advection effect avoiding numerical diffusion, and (iii) to

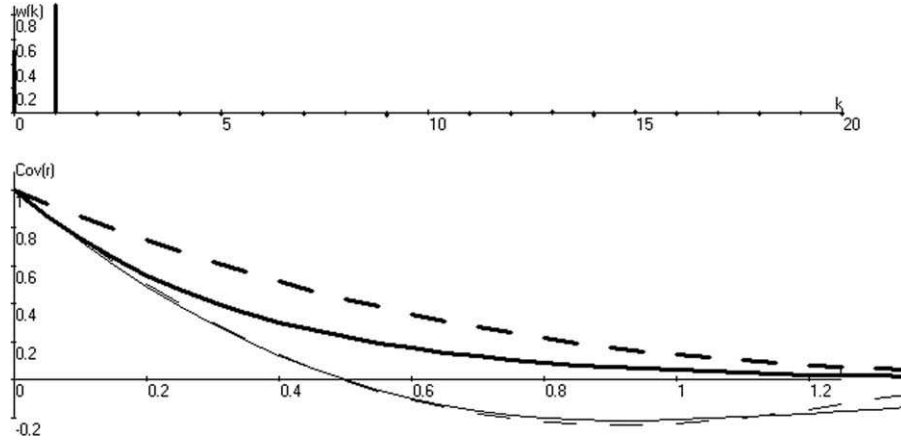


**Figure 1.** Control display showing the set of autoregression weights (top graph) and the fitted covariance functions (bottom graph) for NZR (the same type of graph is displayed also for intermittency). The 3-D structure  $C_{\phi(Y_R)}$  of the non-Gaussian process (bold line) is compared to the 3-D structure  $C_{Y_R}$  of the Gaussian process (bold dashed line) obtained from the Chebyshev-Hermite expansion. The 1-D covariance function  $C_I$  numerically derived according to equation (5) (thin line) is compared to the covariance function  $C_I^*$  approximated from the set of autoregressive weights shown (thin dashed line almost confounded with the thin line). In this illustration, the covariance functions are exponential and the point distribution is an inverse Gaussian with the parameters detailed in the case study (section 7).

delineate rainy versus dry areas. This last issue is dealt in the next section.

### 5.1. Time Anisotropy

[32] In its most basic form, the TBM yields 3-D homogeneous and isotropic Gaussian random fields. So if we apply an anamorphosis

$$R(x, y, z) = \varphi(Y_R(x, y, z)). \quad (17)$$

[33]  $R(x, y, z)$  will also have a covariance function that is isotropic. In our model, two dimensions jointly denoted by  $\mathbf{x}=(x, y)$  are needed to represent the horizontal plane. This plane can be viewed at the ground surface or at any reference level below the bottom of the cloud system producing rain. The third dimension  $z$  can be used as a time dimension  $t$ , assuming that the precipitation system is statistically stationary in space and time, given an appropriate anisotropy. In practice, we introduce the anisotropy through a reference distance  $L$  and a reference duration  $D$  that satisfy:

$$\frac{\delta t}{D} = \frac{\delta x}{L} = \frac{\delta y}{L}. \quad (18)$$

[34] This property is known as the Taylor hypothesis [Taylor, 1938] and was first evidenced experimentally for rainfields by Zawadzki [1973]. The ratio  $U_R = L/D$  has the dimension of a velocity and is termed the Taylor velocity. It should be realized that the Taylor velocity is not a velocity of displacement of the precipitation system. This scalar relates the time and space evolution of rainfall patterns [Gupta and Waymire, 1987]. The above-defined anisotropy “stretches” or “compresses” linearly the  $z$  axis of the 3-D space of the raw TBM simulation and gives an isotropic correlation pattern:

$$C(\mathbf{h}, t) = C_3 \left( \sqrt{\frac{h^2}{L^2} + \frac{t^2}{D^2}} \right), \quad (19)$$

where  $C$  is the covariance function of the rain process in space and time and  $C_3$  is an isotropic 3-D covariance function, and  $h = |\mathbf{h}|$  and  $t$  are space and time distances.

### 5.2. Advection

[35] To avoid numerical diffusion, the proposed simulator accounts for advection during the step of orthogonal backprojection of line processes. The principle consists in backprojecting the line processes along the backtrajectories of “rainfall particles” instead of backprojecting on a regular grid.

[36] The equation of a backtrajectory is the following:

$$\mathbf{x}_1 = \mathbf{x}_0 - \int_{t_0}^{t_1} \mathbf{U}(\mathbf{x}_t, t) dt. \quad (20)$$

[37] One can notice the sign difference with equation (2). In this equation,  $\mathbf{x}_1$  is the place where we find at a time  $t_0$  the rainfall particle that will be at a grid point  $\mathbf{x}_0$  at  $t_1$  given the prevailing advection. Thus, backprojecting the turning bands at point  $\mathbf{x}_1$  at time  $t_1$  allows to generate directly the simulated value  $Y(\mathbf{x}_0, t_1)$  that will actually be at a grid point  $\mathbf{x}_0$  at that time. The backtrajectory must be calculated, either numerically (Runge-Kutta scheme) or analytically, before the simulation can start (Figure 2). We can notice that, in general, (i) the point  $\mathbf{x}_1$  is not on the Eulerian 2-D simulation grid and (ii) the advection field must be prescribed beyond the simulation domain.

[38] Of practical importance is the case of uniform in space and constant in time advection that simply reads

$$\mathbf{x}_1 = \mathbf{x}_0 - \mathbf{U}(t_1 - t_0). \quad (21)$$

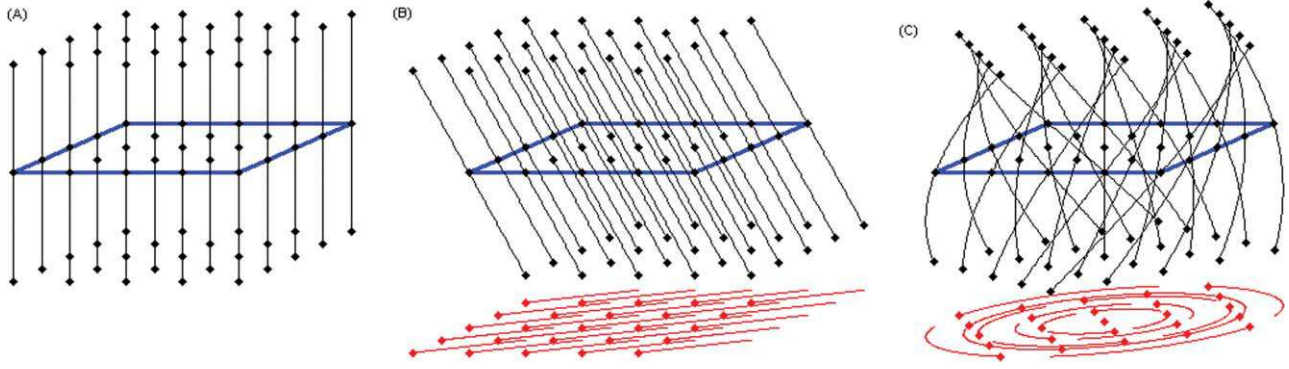


**Figure 2.** Sketchy illustration of (i) the computed 3-D advection backtrajectories where the time axis is vertical and oriented upward and the horizontal geographical plane is drawn in perspective (top graphs) and (ii) the corresponding advection field (bottom graphs in red). The scheme (a) is the space as understood by an Eulerian observer standing at a fixed point  $\mathbf{x}_E$ . The observer grid is represented at a reference time. The simulated points at times before and after the reference time are respectively below and above the grid. The schemes (b) and (c) show, respectively, a left-to-right linear flow and a circular, clockwise vortex flow. Lagrangian observers will move following the advection field plotted below. A backtrajectory describes the positions  $\mathbf{x}_L(t)$  at which are located the Lagrangian observers that will meet at time  $t$  an Eulerian observer standing at  $\mathbf{x}_E$ .

[39] This case coincides with a simple transformation from Lagrangian (subscript  $L$  where needed) to equivalent Eulerian coordinates used in *Lepioufle et al.* [2012, equation (3)], where they consider  $\mathbf{U}$  parallel to the  $x$  axis, with no loss of generality:

$$\begin{cases} x_L = x_E - U.t, \\ y_L = y_E, \\ z_L = t(L/D). \end{cases} \quad (22)$$

[40] In summary, time anisotropy and advection are dealt through coordinate transformation. From any underlying 3-D-isotropic second-order stationary random function defined in  $\mathbf{R}^3$  in Lagrangian coordinates, the choice of  $\mathbf{U}$  and  $U_R$  defines a companion random function in Eulerian coordinates, where one of the three dimensions is converted into a time axis and where a uniform constant advection is introduced. At this stage, the simulator is thus able to simulate advected rainfall fields as follows:

$$R(\mathbf{x}_E, t) = \varphi(Y_R(\mathbf{x}_E - \mathbf{U}.t, t.U_R)) = \varphi(Y_R(\mathbf{x}_L, t.U_R)), \quad (23)$$

where  $\varphi$  is the ad hoc anamorphosis function and  $U_R$  the Taylor velocity.

## 6. Rainfall Intermittency

[41] In SAMPO, the delineation between rainy and dry areas is constructed through an indicator function  $I(\mathbf{x}, t)$  derived by thresholding a Gaussian field  $Y_I(\mathbf{x}, t)$ :

$$I(\mathbf{x}, t) = \mathbf{1}_{Y_I(\mathbf{x}, t) > \lambda}, \quad (24)$$

where the function  $\mathbf{1}$  is binary, equal to 1, when the subscript proposition is true and 0 if not. The time anisotropy

and advection seen in the previous section can be applied to  $I$ . The multiplication of  $I(\mathbf{x}, t)$  by the continuous rainfall field  $R(\mathbf{x}, t)$  expressed in (23) carves the inner variability of the rainy areas according to the intermittency field [see *Barancourt et al.*, 1992]. The threshold used to derive the indicator function from the TBM-generated field is the Gaussian quantile  $\lambda = G^{-1}(F_0)$  corresponding to a dry fraction area  $F_0$ , which is also a nonexceedance probability. The relation between the variogram  $\gamma_{Y_I}$  of the underlying Gaussian field and the variogram  $\gamma_I$  of the binary field got after thresholding is as follows [*Lantuéjoul*, 2002, p. 207]:

$$\gamma_I(h) = \frac{1}{\pi} \int_0^{\arcsin \sqrt{\frac{\gamma_{Y_I}(h)}{2}}} \exp \left[ -\frac{\lambda^2}{2} (1 + \tan^2 t) \right] dt. \quad (25)$$

[42] This one-to-one mapping between the variograms given  $F_0$  has no analytical solution, in general, but is rather easy to invert numerically. It has a role similar to formula (16) for NZR.

[43] In practice, this approach poses questions both about the dependency between the NZR field and the intermittency field and about the dynamics of the intermittency field. In the presented version of SAMPO, the functions  $Y_R$  and  $Y_I$  are generated independently. This option allows a drastic simplification of the simulator and may or may not be supported by data evidence (see discussion below in section 8.2). If needed, different methods exist to generate dependent 3-D random fields (see for instance, *Emery* [2008]) provided the dependency between  $Y_R$  and  $Y_I$  can be qualified. As far as the dynamics of intermittency is concerned, our basic choice is to use the same advection parameters in simulating NZR and the indicator function. More complicated advection patterns can be introduced if needed.

[44] Complementing equation (23), SAMPO generates intermittent advected rainfall fields according to the general expression announced in section 1:

$$R_I(\mathbf{x}_E, t) = \varphi(Y_R(\mathbf{x}_L, t, U_R)) \mathbf{1}_{Y_I(\mathbf{x}_L, t, U_I) \geq \lambda}. \quad (26)$$

[45]  $R_I$  denotes the final advected intermittent field with, in most simple cases,  $\mathbf{x}_L = \mathbf{x}_E - \mathbf{U}t$  where  $\mathbf{U}$  is a constant and homogeneous advection,  $U_R$  and  $U_I$  are the respective Taylor velocities of NZR and intermittency that are usually different.

## 7. Implementation and Illustration Case Study

[46] The flexibility allowed by the basic ingredients of a simulation—variability of the NZR and intermittency fields including Taylor velocity, advection field specification—makes extensive validation difficult. However, a variety of studies conducted using the modular structure of SAMPO helped a step-by-step validation of each module and of several combinations of modules. The dynamic visualization of the simulated fields has been extensively used for troubleshooting.

[47] With the limited intention to illustrate a possible application of SAMPO and to show that the simulated fields are consistent with the specified hypotheses and parameters, we present in this section a case study relying on a data set published by *Emmanuel et al.* [2012, hereinafter E2012]. The C-band weather radar of Treillières (a Météo France instrument close to Nantes, France) provided high-resolution data (5 min, 250 m) considered at a distance of less than 20 km in a rather flat area. These features allowed assuming a good homogeneity of the data regarding possible effects of range dependence and of vertical reflectivity profile. A meteorological analysis partitioned 24 homogeneous sequences taken from 12 recording days in 2009 into four categories of rainfall (see E2012, Table 1). The parameters and the images used in this case study pertain to the so-called category of showers associated to the tail end of oceanic perturbations (Group 2 of E2012). It contains seven rainfall sequences, which represent 104 radar images in total. The space-time structure of the set of images has the following characteristics (for NZR, see E2012, Figures 7 and 8). The identified space ranges are about 5 km for the NZR and 20 km for the intermittency. A Lagrangian assessment of the NZR time range, i.e., after removing advection sequence per sequence, yields 20 min. For the intermittency this range is not easy to assess because the life duration of rainy areas is usually greater than the time they need to cross the observation domain. Based on the slope of the variogram at the origin, we took for intermittency a time range of 195 min. The above values correspond to Taylor velocities of respectively 4.16 and 1.71  $\text{ms}^{-1}$  for NZR and intermittency. For the considered category of rainfall, (i) the expected value and the standard deviation of NZR are, respectively, equal to 6.05 and 17.9  $\text{mm h}^{-1}$ , (ii) the probability of rain is 36.2%, and (iii) NZR and intermittency fields are weakly correlated.

[48] We simulated 1000 independent rainfall sequences of 12 h over a domain of  $80 \times 80 \text{ km}^2$  representing 1000 volumes of size  $(81 \times 81 \times 145)$  with space and time units

of, respectively, 1 km and 5 min. No mathematical or software issue except computation time prevents from choosing any other spatial resolution or domain size. The space-time variograms are exponential. The point distribution of NZR is an inverse Gaussian that is taken constant in space and time, with the parameter values given above. The rainfall category being rather heterogeneous in term of advection field, we took a set of representative advection velocities (0, 2, 4, 8, and 16  $\text{ms}^{-1}$ ) arbitrarily oriented northward and applied to both intermittency and NZR. The rainfall values generated at 5 min time steps are accumulated over 15 and 30 min and 1 and 3 h.

[49] Figure 3 shows first the variograms prescribed to the simulator. The size of the radar data domain was obviously too small to identify directly the life duration of the rainy areas (range of the Lagrangian time variogram beyond the maximum distance). Also in the simulated fields, the ranges of the space and temporal indicator variograms are close to the domain size, and each field is highly autocorrelated. The NZR variability occurs at smaller time and spatial ranges. On Figure 3, we plotted the dispersion of the 5 min variograms derived from the 1000 generated sequences. Basically, two comments can be made about the remarkable average fit and the dispersion of the 5 min variograms of the individual sequences.

[50] The average value of the generated variograms is close to the space and time variograms prescribed for the non-Gaussian process, which proves the consistency of the simulator in regard to the space-time structure. Both are significantly far from the variogram models used to generate the Gaussian values, which confirms the benefit of using anamorphosed structure functions. A closer look nevertheless reveals some minor discrepancies between generated and prescribed variograms at medium- to long range for intermittency fields. This lack of convergence could be linked to the life duration of rain areas.

[51] The dispersion of the generated variograms is substantial, which shows the potential uncertainty of the structure analysis in relation with the size of the sampling domain compared to the range of the phenomenon. The dispersion is almost symmetric for NZR and slightly asymmetric for the intermittency by construction. All these elements governing the rainfall variability are embedded in the simulation and can be transmitted to downstream studies on hydrometeorological variability and its propagation in hydrology.

[52] Figure 4 brings validation elements about the choice of the distribution function. The inverse Gaussian appears to fit well the radar data and the generated data as well. The radar data set is affected by digitization but still follows fairly well the theoretical distribution up to its largest values, around 60 mm in 5 min. The simulated values are aligned with theoretical quantiles up to the largest intensities. The extreme values have been checked through other sets of simulation to alternate in a balanced way overestimations and underestimations of the highest quantiles for sampling reasons.

[53] The anamorphosis transformation works apparently well both to reproduce a correct distribution of the generated values and to identify the variograms of the underlying Gaussian process.

[54] Figure 5 puts the final product of the simulator in front of a radar image extracted from the study period.



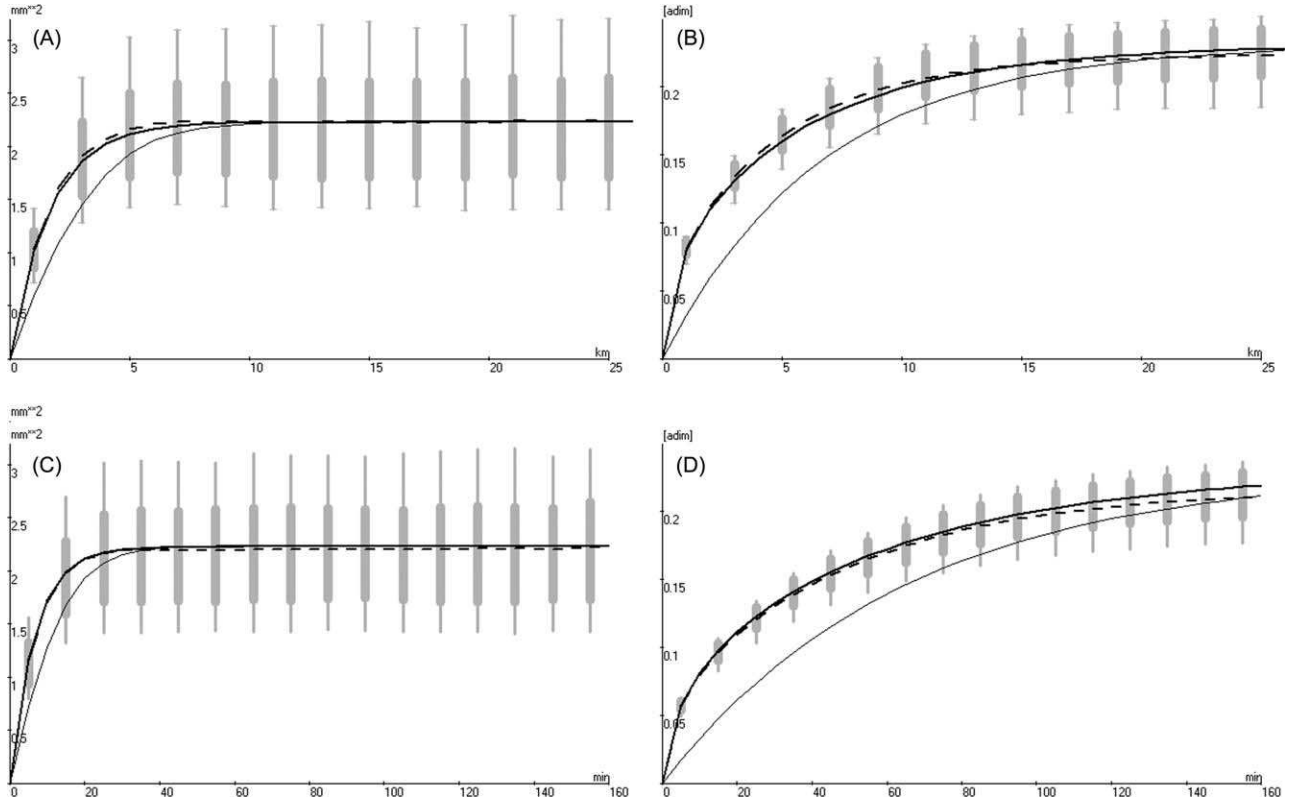


**Figure 3.** (a and b) Space and (c and d) time variograms of NZR (Figures 3a and 3c) and intermittency (Figures 3b and 3d) computed from the case study simulations (shower-type rainfall seen by the radar of Treillières, France). Each graph shows the theoretical variogram fitted to the non-Gaussian radar field (continuous line), the variogram of the underlying Gaussian process used by the simulator (thin line), and the average variogram deduced from the simulated data (dashed line). The time variograms are Lagrangian for both experimental and theoretical forms, i.e., computed without advection. The boxplots show the median, interquartile, and interdecile values taken by the experimental variograms of the simulated fields (1000 sequences of 12 h at 5 min time step).

Beyond the above inspection of the replication of the prescribed statistical properties (distribution and structure), putting together simulated and radar images calls complementary comments. This juxtaposition lacks simultaneity because the simulation is not conditional. At the elemental time step (5 min), the simulation looks realistic in terms of granularity of NZR and size of the intermittency patterns. Still, the simulation looks slightly too fragmented compared to the radar image that is organized in more compact bands. This difference is important but understandable since no anisotropy in space was prescribed to intermittency fields (see section 8.3 for a simulation with bands). One can notice concentric alignments in the radar image that are related to remaining mask effects and that, of course, are absent from the simulation, which is homogeneous by construction.

## 8. Hypothesis Testing

[55] One possible application of a simulator like SAMPO is to explore how empirically known properties of rainfall field variograms are related to basic hypotheses included in the simulator. We develop two examples (see later) of such hypothesis testing pertaining to (i) the variogram range increase with time accumulation and (ii) the dependency

between intermittency and NZR variability. We illustrate next how Taylor velocity and advection combine together to reproduce rainfield kinematics.

### 8.1. Variography of Cumulated Rainfall Fields

[56] Experimental studies showed that the ranges and sills of experimental variograms evolve with rainfall accumulation duration (see for instance, *Lebel et al.* [1987, Figure 2]). Presenting space and time experimental variograms computed for different accumulation durations with the parameter setting of the case study (see section 7), Figure 6 shows how the range and the sill are influenced in a similar way by increasing accumulation times and advection velocities. The aforementioned empirical property may thus result from both factors.

[57] The sills of the space and time variograms decrease with the accumulation duration at a common rate in all directions (Figures 6a and 6c). We find here the effect of the so-called regularization of a random variable over time [see *Journal and Huijbregts*, 1978; *Bacchi and Kottegoda*, 1995; *Lepioufle et al.*, 2012].

[58] While the range of the variograms in time and space remains constant at different durations when there is no advection (i.e., in the WE direction), we observe different

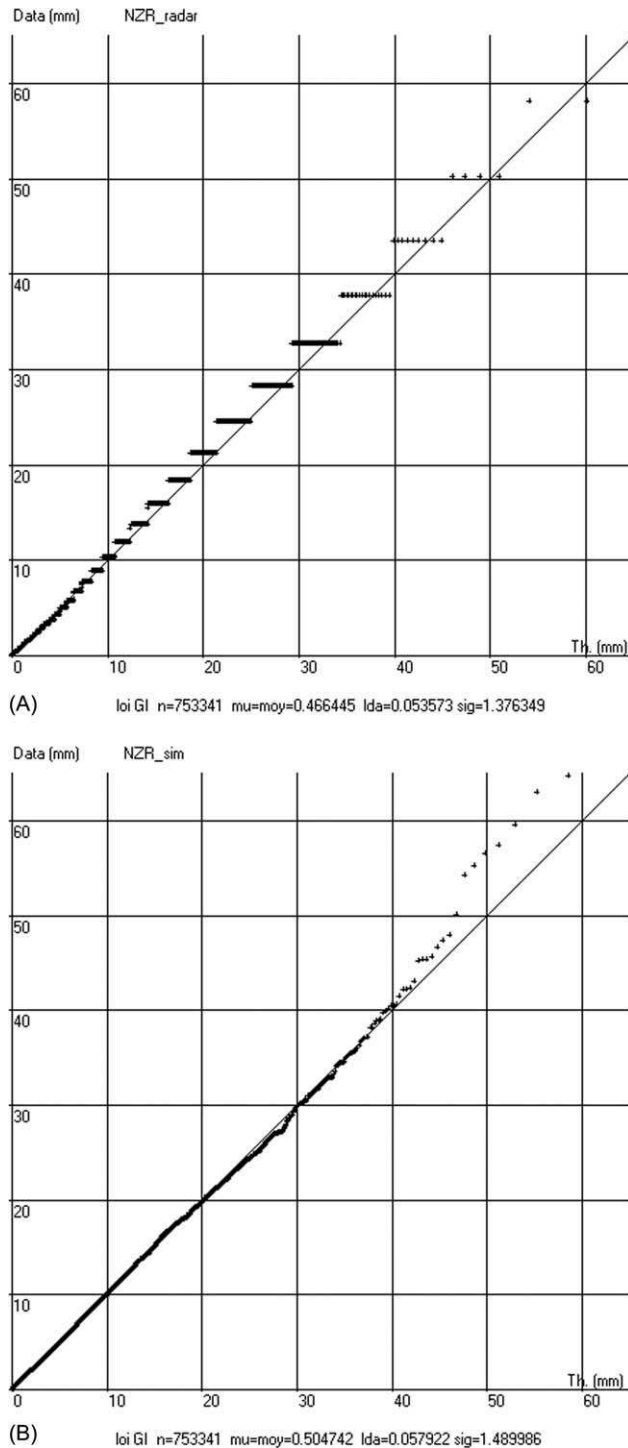


**Figure 4.** Plots of the theoretical quantiles from an inverse Gaussian distribution versus the sample quantiles of (a)  $\sim 7 \times 10^5$  radar NZR data and (b) an equal number of NZR values sampled in the simulated rainfall fields.

effects in space and time when advection is activated (visible in the NS direction). The space range increases with the accumulation duration in the advection direction (see Figure 6c). The “advected” variogram has a weaker slope at the origin than the orthogonal one (WE), and it reaches their common sill significantly farther (7 km range at 15 min to

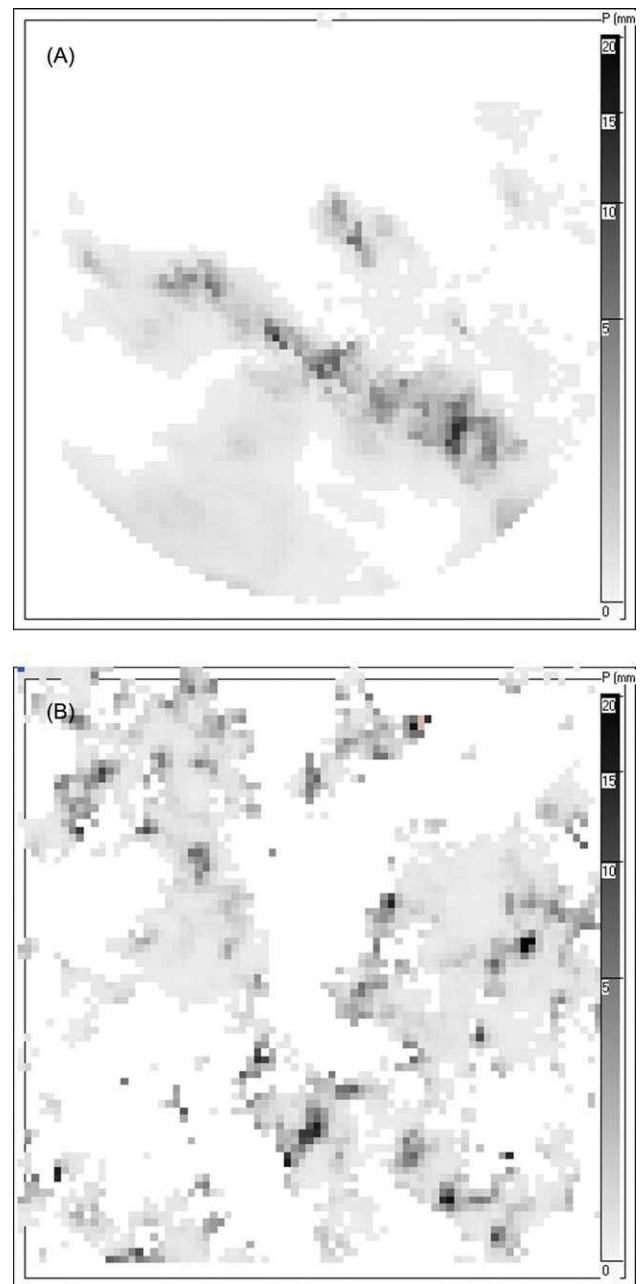


**Figure 5.** Juxtaposition of (a) a typical radar image and (b) a simulated rainfall field taken at the 5-minute elemental time step of the study. The space resolution is 1 km.

almost 25 km for 1 h). The same comment applies to space variograms at increasing advection velocities (see Figure 6d). One can notice that for advection velocities of  $8 \text{ m s}^{-1}$  and above, the NS space variogram undulates with an  $\sim 5 \text{ km}$  period close to the range of the elemental NZR variogram. This undesirable lack of continuity in the simulated rainfields comes from a too coarse time resolution in regard to the advection of the field given the space resolution. The time range also tends to increase with the duration at a given advection velocity (see Figure 6a). But, when advection velocity increases, the time range of the variogram decreases as advection favors the renewal rate of the rainfield as experienced by a Eulerian observer (see Figure 6b). We see here

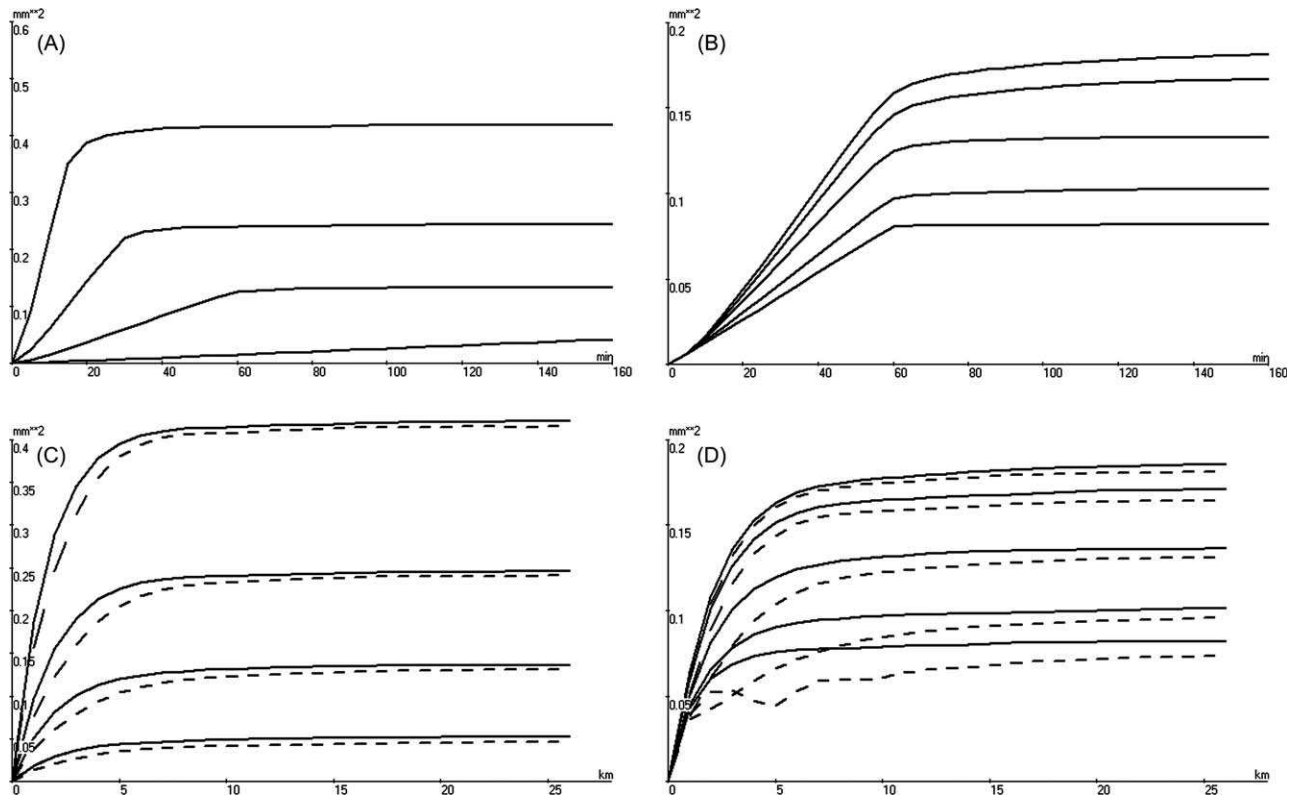


**Figure 6.** (a and b) Time and (c and d) space variograms computed from the case study simulations. Space variograms distinguish WE direction (solid line) from NS direction (dashed line). On the left hand side (Figures 6a and 6c), four accumulation durations (15, 30 min, 1 and 3 h) are considered for an advection velocity of  $4 \text{ m s}^{-1}$ . On the right hand side (Figures 6b and 6d), five advection velocities (0, 2, 4, 8, and  $16 \text{ m s}^{-1}$ ) are considered for accumulation duration of 1 h. The sill of the variograms monotonously decreases with both the duration and the advection velocity, allowing the unambiguous identification of the curves in each graph.

that the smoothing effect of advection is anisotropic [Lepoulle et al., 2012].

## 8.2. Intermittency and NZR Dependency

[59] By construction, the simulator considers NZR variability as independent of the shape of the rainy areas at the elemental time step of simulation, which is of 5 min in the present case study simulation. Figure 7 shows time and space transition variograms, which are computed selecting the couples of points being respectively in and out of rainy areas and which measure the dependency between intermittency and NZR. The Dirac shape of the transition variograms corresponding to the elemental time step of simulation complies with the basic design of the simulator. The small apparent range at lag 1 in both space and time is due to the grid cell size (1 km, 5 min). Figure 7 also shows that this independence vanishes both in time and space as soon as rainfields are accumulated over two elemental time steps. Advection is a secondary factor destroying independence. As any type of rain sensor “integrates” either in time or space or both, our conclusion is that this independence property is kind of fleeting, as it tends to disappear as soon as we take a measurement. This result shades a new light on this hypothesis and, in any case, is not in contradiction with earlier works that evidenced a significant dependency at

greater than hourly time scales (see for instance, Barancourt et al. [1992] or Braud et al. [1994] at hourly time scale or Herr and Krysztofowicz [2005] and Bardossy and Pegram [2009] at daily time steps).

[60] In practice, we recommend the following. In the case where the “elemental step” is such that the independence is not valid, we indicated that the cosimulation of the two related fields is possible via the same TBM approach [see Emery, 2008]. In the case where the independence assumption can be made (like in the case study proposed section 7), we recommend using it for the sake of simplicity, as long as the integrated values of the simulated rainfall intensities exhibit the desired properties of dependency.

## 8.3. Rainfall Field Kinematics Through Taylor Velocity and Advection

[61] From a physical point of view, the difference between the two velocities is the classical one between advection and diffusion or flow velocity and turbulence. They have very distinct visual effects on the rainfall field kinematics—one is modifying the shape of the field while the other one moves this shape in a recognizable direction. They are consistent with what radar detection shows.

[62] Figure 8 illustrates the combined effect of advection and Taylor velocity in a case of banded convection,

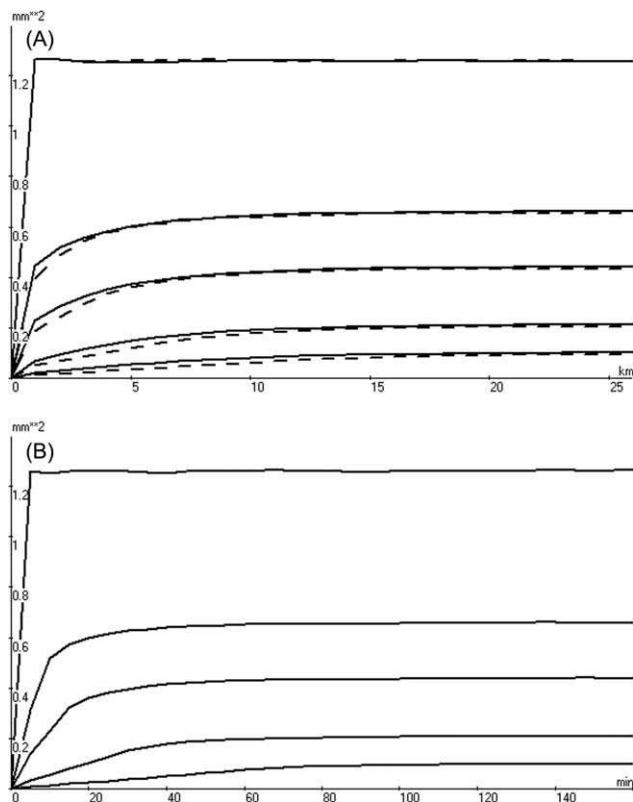


**Figure 7.** (a) Space and (b) time transition variograms computed from the case study simulations for five accumulation durations (5 min, the elemental simulation time step, as well as 10, 15, 30, 60 min). For space, the NS (dashed lines) and WE (solid lines) directions are distinguished. The advection velocity is  $4 \text{ m s}^{-1}$  and oriented north. The sill of the variograms decreases with the duration, allowing unambiguous identification of the curves.

mimicking the radar sequence used in the previous section. We kept basically all the parameters identical. An anisotropy factor 4 in the N-105-E direction is applied to the intermittency field, leading to modify the space and time variogram ranges in order to preserve the Taylor velocity. The advection is perpendicular to the bands (oriented N-15-E) and is equal to  $4 \text{ ms}^{-1}$ . The short sequence displayed Figure 8 shows how the renewal rates of the elemental rainfall structures—intermittency and NZR—combine with the advection velocity giving the general motion. The rainy areas are relatively stable in regard to their advection and the NZR fluctuations are relatively fast in regard to the shape of the rainy areas. The intermittency field clearly organizes the rainfield in bands that are advected and renewed in time. The rain cells inside the rainy areas are evolving with their own dynamics. Both elements conjugate to simulate the birth and development of new rain bands (northwest sector).

## 9. Conclusion

[63] In this study, we adapted the classical TBM to precipitation simulation in space and time. The merits of the TBM are the speed of computation (simulation in 1-D instead of 3-D), the flexibility (space distortion for instance

to introduce advection and diffusion) and the easiness of parameter prescription (basically Taylor velocity and advection in addition to classical statistical parameters of mean and variance). The main adaptations proposed in this study concern (1) the advection of the precipitation fields by the prevailing winds, (2) the skewness of the marginal distribution of precipitation rates, (3) the intermittency of rainfall in time and space, and (4) the space-time anisotropy of the rainfall process.

[64] The notion of backtrajectories introduced in the heart of the TBM design allows the direct simulation of potentially very diverse advected fields and avoids numerical diffusion. Illustrative runs confirm that advection velocity has a major effect on the statistical properties of rainfall accumulation.

[65] The use of Chebyshev-Hermite polynomial expansions clarifies the link between the desired structure of the non-Gaussian generated fields and the Gaussian generating process of the TBM lines. The optimization of the weighting system is simplified and the computation of the anamorphosis is more tractable. Control plots (Figure 1) show this correction is accurate and needed, as the amplitude between Gaussian and non-Gaussian covariances reaches up to 30% in the study case.

[66] The definition of intermittency as a binary process statistically independent of NZR variability allows a drastic simplification of its implementation in the simulator. Illustrative runs show that the independence rapidly vanishes after accumulation and that advection accentuate this process. This hypothesis is thus not exclusive of earlier experimental studies, showing dependency for rainfall accumulations more than 1 h.

[67] The space-time anisotropy captures important details of the precipitation dynamics summarized by the Taylor velocity. Featuring the lifetime and size of elementary rainfall cells The Taylor velocity of NZR, relating the lifetime and the size of elementary rainfall cells, determines the renewal rate of the internal structures of the rainy areas. The Taylor velocity of the intermittency governs the renewal rate of the rainy areas themselves. The combined role of these velocities with the advection velocity proves to produce flexible enough rainfall field kinematics.

[68] Practical applications of the SAMPO simulator that contributed to build and test its different modules include the development of a rainfall error model to study hydrological uncertainty [Renard *et al.*, 2011], the Lagrangian analysis of radar rainfall fields [Emmanuel *et al.*, 2012], and teaching support.

[69] Current developments are oriented toward (i) conditional simulations given prescribed rain gauge data sets, (ii) rainfall type sequencing in relation with meteorological data, or (iii) nonstationarity under orographic conditions. In many hydrological applications, the uncertainty introduced by gauge network sampling is a still open question and simulations conditioned to gauge readings can help assessing measurement errors. Under middle European climate, the simulation of the occurrence and type of rainy weather situations is compulsory to produce long series of rainfall data. Under orographic influence the mean and variance values of NZR and intermittency vary in space and the advection field becomes more complex.

[70] To this end and far from an exclusive choice between conservation laws and observed statistics, we



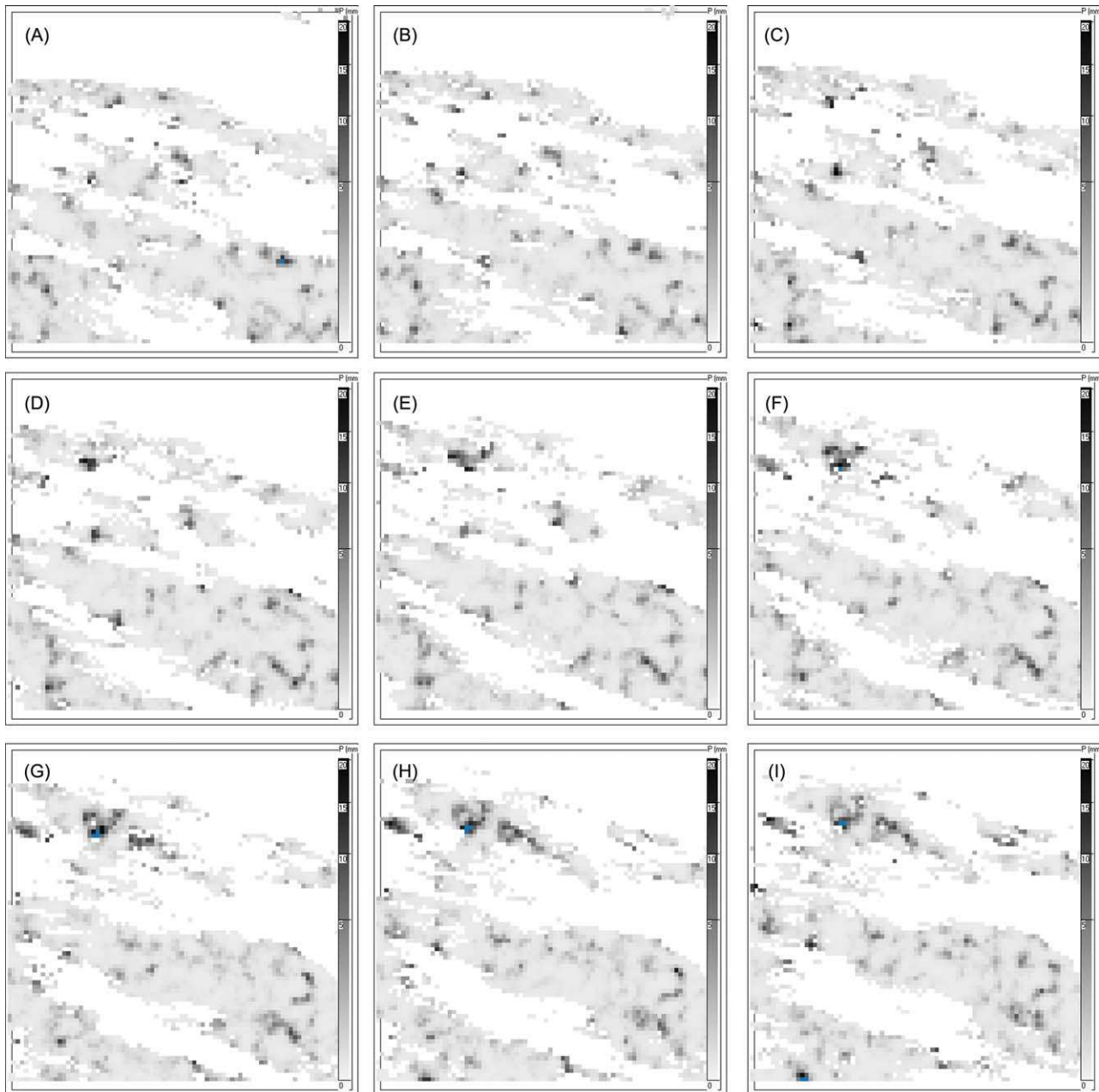


**Figure 8.** Sequence of 5 min rainfall fields simulated with the parameters of the case study slightly modified to obtain banded convection (intermittency anisotropy of factor 4 in the N-105-E direction). The  $4 \text{ ms}^{-1}$  advection is heading N-15-E.

consider that there is a better link to seek between physically based meteorological models and stochastic simulation models. The introduction of the advection field in our simulator is a first step that we want to repeat about rainfall and weather-type sequencing and orography.

[71] **Acknowledgments.** The development of this simulator benefited much along the years from the involvement of colleagues and Ph.D. students, especially I. Braud, K. Engeland, J.-M. Lepioufle, M.H. Ramos, and B. Renard. The authors acknowledge the financial supports from Irstea, EDF, CNRS, ANR, CCR, CG92 (France), and SINTEF (Norway). The authors are very grateful to I. Emmanuel, H. Andrieu, and B. Flahaut (IFSTTAR Nantes) for their help in selecting the case study. The presented formulation of the model much benefited from discussions with C. Lantuéjoul (ENSM, Paris).

The authors recognize the full worth of the contribution of the anonymous reviewers to the quality of the paper.

## References

- Amoroch, J., and B. Wu (1977), Mathematical models for the simulation of cyclonic storm sequences and precipitation fields, *J. Hydrol.*, 32(3-4), 329–345.
- Armstrong, M. (1992), Positive definiteness is not enough, *Math. Geol.*, 24(1), 135–143.
- Arnell, N. W. (1999), Climate change and global water resources, *Global Environ. Change*, 9(supplement 1), S31–S49.
- Austin, G. L., and A. Bellon (1974), The use of digital weather radar records for short-term precipitation forecasting, *Q. J. R. Meteorol. Soc.*, 100, 658–664.
- Bacchi, B., and N. T. Kottegoda (1995), Identification and calibration of spatial correlation patterns of rainfall, *J. Hydrol.*, 165(1-4), 311–348.

- Barancourt, C., J. D. Creutin, and J. Rivoirard (1992), A method for delineating and estimating rainfall fields, *Water Resour. Res.*, 28(4), 1133–1144.
- Bardossy, A. (2011), Interpolation of groundwater quality parameters with some values below the detection limit, *Hydrol. Earth Syst. Sci.*, 15, 2763–2775.
- Bardossy, A., and G. Pegram (2009), Copula based multisite model for daily precipitation simulation, *Hydrol. Earth Syst. Sci.*, 13(12), 2299.
- Bell, T.L. (1987), A space-time stochastic model of rainfall for satellite remote-sensing studies, *J. Geophys. Res.*, 92(D8): 9631–9643.
- Bellin, A., and Y. Rubin (1996), HYDRO\_GEN: A spatially distributed random field generator for correlated properties, *Stochastic Hydrol. Hydraul.*, 10(4), 253–278.
- Boé, J., L. Terray, E. Martin, and F. Habets (2009), Projected changes in components of the hydrological cycle in French river basins during the 21st century, *Water Resour. Res.*, 45(8), W08426.
- Braud, I., P. Crochet, and J. D. Creutin (1994), A method for estimating mean areal rainfall from binary satellite information, *J. Appl. Meteorol.*, 33(12), 1551–1561.
- Chhikara, R. S., and J. L. Folks (1974), Estimation of Inverse Gaussian distribution function, *J. Am. Stat. Assoc.*, 69(345), 250–254.
- Emery, X. (2008), A turning bands program for conditional co-simulation of cross-correlated Gaussian random fields, *Comput. Geosci.*, 34, 1850–1862.
- Emery, X., and C. Lantuéjoul (2006), TBSIM: A computer program for conditional simulation of three-dimensional Gaussian random fields via the turning bands method, *Comput. Geosci.*, 32(10), 1615–1628.
- Emmanuel, I., H. Andrieu, E. Leblois, and B. Flahaut (2012), Temporal and spatial variability of rainfall at the urban hydrological scale, *J. Hydrol.*, 430–431, 162–172.
- Folks, J. L., and R. S. Chhikara (1978), Inverse Gaussian distribution and its statistical application—Review, *J. R. Stat. Soc. Ser. B*, 40(3), 263–289.
- Galli, A., H. Beucher, G. Le Loc'h, and B. Doligez (1994), The pros and cons of the truncated Gaussian method, *Geostat. Simul.*, 7, 217–233.
- Guillot, G. (1999), Approximation of Sahelian rainfall fields with meta-Gaussian random functions. Part 1: model definition and methodology, *Stochastic Environ. Res. Risk Assess.*, 13, 100–112.
- Gupta, V. K., and E. Waymire (1987), On Taylor's hypothesis and dissipation in rainfall, *J. Geophys. Res.*, 92(D8), 9657–9660.
- Gupta, V. K., S. L. Castro, and T. M. Over (1996), On scaling exponents of spatial peak flows from rainfall and river network geometry, *J. Hydrol.*, 187(1–2), 81–104.
- Halton, J. (1964), Algorithm 247: Radical-inverse quasi-random point sequence, *Commun. ACM*, 7, 701–702, doi:10.1145/355588.365104.
- Herr, H. D., and R. Krzysztofowicz (2005), Generic probability distribution of rainfall in space: the bivariate model, *J. Hydrol.*, 306(1–4), 234–263.
- Journel, A. G., and C. J. Huijbregts (1978), *Mining Geostatistics*, 600 pp., Academic, London.
- Lantuéjoul, C. (2002), *Geostatistical Simulation: Models and Algorithms*, 256 pp., Springer, Berlin.
- Lebel, T., G. Bastin, C. Obled, and J. D. Creutin (1987), On the accuracy of areal rainfall estimation: A case study, *Water Resour. Res.*, 23(11), 2123–2134.
- Lepioufle, J.-M., E. Leblois, and J.-D. Creutin (2012), Variography of rainfall accumulation in presence of advection, *J. Hydrol.*, 464–465, 494–504.
- Mandapaka, P. V., W. F. Krajewski, R. Mantilla, and V. K. Gupta (2009), Dissecting the effect of rainfall variability on the statistical structure of peak flows, *Adv. Water Resour.*, 32(10), 1508–1525.
- Mantoglou, A., and J. L. Wilson (1982), The turning bands method for simulation of random fields using line generation by a spectral method, *Water Resour. Res.*, 18(5), 1379–1394.
- Matheron, G. (1973), The intrinsic random functions and their applications, *Adv. Appl. Probab.*, 5, 439–468.
- Matheron, G. (1989), The internal consistency of models in geostatistics, in *Geostatistics*, edited by M. Armstrong, pp. 21–38, Kluwer Acad., Dordrecht.
- Mejia, J., and I. Rodriguez-Iturbe (1974), On the synthesis of random fields sampling from the spectrum: An application to the generation of hydrologic spatial processes, *Water Resour. Res.*, 10, 705–711.
- Menabde, M., and M. Sivapalan (2001), Linking space-time variability of river runoff and rainfall fields: A dynamic approach, *Adv. Water Resour.*, 24(9–10), 1001–1014.
- Mezghani, A., and B. Hingray (2009), A combined downscaling-disaggregation weather generator for stochastic generation of multisite hourly weather variables over complex terrain: Development and multi-scale validation for the Upper Rhone River basin, *J. Hydrol.*, 377(3–4), 245–260.
- Niemczynowicz, J. (1988), The rainfall movement—A valuable complement to short-term rainfall data, *J. Hydrol.*, 104(1–4), 311–326.
- Renard, B., D. Kavetski, E. Leblois, M. A. Thyer, G. Kuczera, and S. W. Franks (2011), Towards a reliable decomposition of predictive uncertainty in hydrological modeling: Characterizing rainfall errors using conditional simulation, *Water Resour. Res.*, 47, W11516, doi:10.1029/2011WR010643.
- Taylor, G. I. (1938), The spectrum of turbulence, *Proc. R. Soc. London Ser. A*, 164(919), 476–490.
- Van der Geest, P. A. G. (1998), An algorithm to generate samples of multivariate distributions with correlated marginals, *Comput. Stat. Data Anal.*, 27, 271–289.
- Vio, R., P. Andreani, and W. Wamsteker (2001), Numerical simulation of non-Gaussian random fields with prescribed correlation structure, *Publ. Astron. Soc. Pacific*, 113(786), 1009–1020.
- Vio, R., P. Andreani, L. Tenorio, and W. Wamsteker (2002), Numerical simulation of non-Gaussian random fields with prescribed marginal distributions and cross-correlation structure. II. Multivariate random fields, *Publ. Astron. Soc. Pacific*, 114(801), 1281–1289.
- Vischel, T., T. Lebel, S. Massuel, and B. Cappelaere (2009), Conditional simulation schemes of rain fields and their application to rainfall-runoff modeling studies in the Sahel, *J. Hydrol.*, 375(1–2), 273–286.
- Zawadzki, I. (1973), Statistical properties of precipitation patterns, *J. Appl. Meteorol.*, 12, 459–472.